https://doi.org/10.5194/egusphere-2026-2569
Preprint. Discussion started: 5 June 2026

New high resolution sea ice leads and floes classification in the CNES SWOT product

Gwenael Jestin[1], Sara Fleury[1], Matthias Raynal[2], Marta Alves[3], Fanny Piras[3], Anaëlle Treboutte[3], François Boy[2], Ines Benabdillah[2], Louise Yu[2], and Gérald Dibarboure[2]

[1]LEGOS, Université de Toulouse, IRD, CNES, CNRS, UPS, Toulouse, France
[2]CNES, Ramonville Saint Agne, 31520, France
[3]Collecte Localisation Satellites, 31520, Ramonville-Saint-Agne, France

Correspondence: Gwenael Jestin (gwenael.jestin@utoulouse.fr)

Abstract. Global observation of ocean and sea ice dynamics relies heavily on space altimeters. However, due to their high latitudes, which are less covered by space altimeters, and the ice cover, which hide the sea level, polar oceans are still poorly observed and modeled. The SWOT altimeter significantly increases the density and quality of measurements up to 77° latitude, covering the entire Southern Ocean and a large part of the Arctic Ocean. Still, these observations require a distinction to be made between measurements taken on water and measurements taken on ice. The CNES L3 Unsmoothed 250m v2.0.1 product includes a new flag that identifies the type of surface observed for each pixel, enabling processing tailored to the object under study. Here we present the methodology used to calculate this flag and evaluate the results obtained using space imagery, nadir altimetry and OSI SAF concentration products.

1 Introduction

The progress in space altimetry allows us to measure the topography of the oceans with a precision of a few millimeters, revealing numerous physical parameters such as the increase in the level of the seas, the presence of underwater mountains or trenches, the variability of currents and eddies, the laws governing the tides, etc. Nevertheless, this level of precision does not yet cover all of the oceans. The sea ice covering polar oceans is a significant observational barrier, complicating sea level measurements and concealing many physical phenomena from direct investigation.

The Arctic Ocean and the Southern Ocean cover about 14 million and 20 million km^2 respectively. Compared to the 510 million km^2 of all the oceans, they represent only 7% of the total surface area. However, because of their position and their seasonal freezing, these oceans play important roles, whether in relation to the worrying variability of sea ice and its effects on the climate, changes in the stratification and vertical and meridional ocean circulation, effects on the stability of the Antarctic and Greenland ice sheets, or impacts on plankton production and the entire food chain. The gradual disappearance of the summer sea ice in the Arctic will also lead to an increase in maritime activities, requiring a better knowledge of this ocean, if only for safety reasons.

Until now, the physics of the oceans has been observed using 'nadir' space altimeters. These altimeters can measure the height of the ocean approximately every $300\,\mathrm{m}$ along the satellite's path. When the ocean is frozen, these measurements of the

https://doi.org/10.5194/egusphere-2026-2569
Preprint. Discussion started: 5 June 2026

height of the ocean can only be taken in the fractures in the ice, or 'leads', thus drastically limiting the density of measurements of the ocean with gaps of several tens of kilometers between sea level measurements, or even several hundred kilometers where the sea ice is at its densest.

The SWOT satellite, launched at the end of 2022, is equipped with KaRIn, the first space altimeter capable of measuring heights over a swath. This $120\,\mathrm{km}$ wide swath provides topographic surveys of the ocean surface in the form of continuous 3D images along the satellite's orbit with a posting of 250 meters. This new technology makes it possible to detect and measure the sea level in all the leads in the swath over ice-covered ocean. It is as if hundreds of nadir altimeters were flying in a line $250\,\mathrm{m}$ apart, thus increasing the number of leads statistically observed along a track. In addition, these measurements, provided in a single image, make it possible to observe the contours of the leads and the ice floes and evaluate the ice concentration.

The sea level measurements in this collection of leads will enable us to significantly improve our knowledge of the polar ocean dynamics. Measuring the floes height above the water level will provide information on the thickness of the sea ice and snow layer, and therefore on its health and volume variations. These measurements will provide a better understanding of the sea ice dynamics and, combined with models, should significantly improve forecasts of its evolution at short and medium term, whether for climate forecasts or for navigation assistance.

After a presentation of SWOT and the products already available, in this article we present the methodology used to identify leads and floes in SWOT altimetric images as well as the new parameters that deliver this information in version 2 of the CNES L3 250m product. The presentation of the results is followed by a series of qualitative or quantitative validations, compared with sea ice classification obtained by the ICESat-2 / Sentinel-3 nadir altimeters and MODIS imager, and with sea ice concentration obtained by space radiometry. The known limitations, planned evolutions and perspectives are discussed in the last section before the concluding synthesis.

2 SWOT and datasets used

2.1 SWOT mission

The SWOT satellite is a NASA/CNES mission developed in participation with CNSA/UKSA and launched in December 2022. During the first six months, the SWOT satellite was placed over a 1-day repeated orbit (period referred to as CalVal phase) to ease the calibration and validation activities. In July 2023 the satellite was moved to its final 21-days repeated orbit (also referred to as Science orbit or phase).

The main instrument of the SWOT payload is the Ka-band Radar Interferometer (KaRIn), a significant technological innovation as it provides for the first time 2D information on topography measurements, covering $50\,\mathrm{km}$-wide swaths on each side of the track. A conventional Ku nadir altimeter (LRM), Poseidon-3C, complements these measurements at the centre of the track (Figure 1).

From the KaRIn measurements the SWOT mission center, operated at CNES, produces Low Resolution (LR) and High Resolution (HR) products. The HR products are dedicated to the monitoring of inland waters and thus geographically limited to continental and coastal surfaces (with punctual acquisitions over open and polar ocean). The LR products are dedicated to

https://doi.org/10.5194/egusphere-2026-2569
Preprint. Discussion started: 5 June 2026

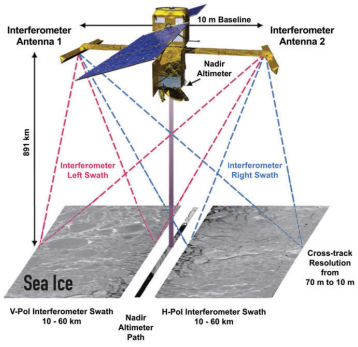

Figure 1. The SWOT mission with the Ku nadir altimeter (not used in this study) and the right and left swaths of the KaRIn altimeter [From Kacimi et al. (2025)].

oceanography studies and applications, and are produced at global scales. A part of the LR processing is performed onboard the satellite to reduce the size of the data downlinked. The highest spatial resolution, available in the L2 LR Unsmoothed products, is of about $500\,\mathrm{m}$ for a posting of $250\,\mathrm{m}$ per $250\,\mathrm{m}$. An additional filtering is applied to produce the L2 LR Expert products, used by most of the oceanography community, at a spatial resolution of $2\,\mathrm{km}$ ($2\mathrm{x}2\,\mathrm{km}^2$ pixels).

First results over open ocean showed an excellent signal to noise ratio, with a random error of about $0.8\,\mathrm{cm}$ for a pixel of $1\,\mathrm{km}^2$ [Peral et al. (2024), Wang et al. (2022)]. By way of comparison, for SARM nadir altimetry, the random error for a single measurement (over open ocean) is of about $3\,\mathrm{cm}$ to $5\,\mathrm{cm}$ depending on the mission [Dinardo et al. (2024), Jiang et al. (2023)], for a footprint area of about $3.6\,\mathrm{km}^2$ (~$12\,\mathrm{km}$ in cross-track direction and ~$300\,\mathrm{m}$ in along track direction). This figure, for nadir altimetry, is even higher over complex inhomogeneous surfaces. The combination of these properties offer an unprecedented context to complete the existing observations and fill the limitations of the current nadir altimeter constellation.

The first topography images on sea ice showed promising initial results exceeding expectations, even though sea-ice observation is not part of the mission's primary objectives. Despite a limited coverage at highest latitudes (SWOT's orbit inclination is of 77.6°), these first results open unforeseen opportunities to complete current remote sensing observations over sea ice regions, in particular to contribute to the sea ice thickness estimation and the observation of the polar oceans. In addition, because the surface height retrieved from KaRIn measurements does not require any physical nor empirical retracker (as it is the case to exploit the backscattered signal measured from nadir altimeters), SWOT also presents the opportunity to provide reference measurements that could be useful for R&D activities on the nadir signal processing. Finally, it's worth underlying that the KaRIn instrument operates in Ka-band, which is an important characteristic to complete the SARAL/AltiKa measurements [Verron et al. (2015)], improve the snow depth observations (that can be estimated from Ku/Ka bands residuals), and prepare the future CRISTAL mission (which will onboard a Ku/Ka bands SAR altimeter [Kern et al. (2020)]).

https://doi.org/10.5194/egusphere-2026-2569
Preprint. Discussion started: 5 June 2026

2.2 Data used in this study

The first images of sea ice from the L2 LR Expert product at $2\,\mathrm{km}^2$ quickly revealed SWOT's impressive potential in measuring this surface. But a more detailed analysis showed that the L2 LR Unsmoothed product at $250\,\mathrm{m}$ allowed even finer structures to be observed such as thin leads in regions of high ice concentration. As these products were initially designed for instrumental and processing expert usages only, they contain limited information to retrieve a precise surface height (no calibration for the systematic errors, not all the geophysical corrections are available to retrieve Sea Surface Height Anomaly (SSHA), . . .). This prevents them from being used without extensive post-processing to recover the missing information. To overcome this limitation, we used the SWOT L3_LR_SSH product, derived from the L2 SWOT KaRIn low rate ocean data products (NASA/JPL and CNES), produced and made freely available by the AVISO and DUACS teams as part of the DESMOS Science Team project (all the details about the standards used are available on AVISO (2024)).

The sea ice classification was based on version 1 of this product, which offered three relevant parameters: SSHA, sigma 0 and total coherence. The latter, being highly correlated with sigma 0 was discarded. The classification is therefore based exclusively on SSHA and sigma 0 identified as the variables duacs_ssha_karin_2_calibrated and sig0_karin_2 respectively. We also used the sea ice concentration parameter derived from EUMETSAT/OSI SAF daily concentration maps to focus our processing on the ice-covered ocean and check the large-scale consistency of our results. This first version also showed frequent slopes on the SSHA transverse to the track due to difficulties in calibrating the altimeter roll above the sea ice. This problem has been largely corrected in version 2 (see [Dibarboure et al. (2022), Ubelmann et al. (2024)] for the L3 calibration).

On top of providing a fully corrected SSHA retrieved from the latest standards for the geophysical corrections (see the product handbook for more information), the correction of the KaRIn systematic errors does not depend on the number of available KaRIn/KaRIn crossovers as it is the case at L2. The L3 calibration [Dibarboure et al. (2022), Ubelmann et al. (2024)] relies on the global multi-mission maps of surface topography, resulting in a more robust and accurate correction for sea ice application based on the KaRIn topography.

Figure 2 shows the two inputs of the classification algorithm for all ascending passes between 28 March and 10 April 2024 around Banks Island and offshore towards the Beaufort Gyre. Residual variability in these parameters is observed above the sea ice from one pass to another and sometimes on the same pass. In the image on the left, we can observe a global upward slope in SSHA from left to right, with a difference in height of more than $30\,\mathrm{cm}$, here probably due to the recent swelling of the Beaufort Gyre not observed in the 1993-2021 Hybrid Mean Sea Surface (MSS) used for SWOT [Laloue et al. (2025)]. While the ice floes emerge above the water only by a few centimeters or tens of centimeters, these differences in height make it very difficult to distinguish between the two surfaces. In the image on the right, sigma 0 is relatively homogeneous over the ice floes, but the very high specularity of the leads can produce extreme variations in backscatter over these surfaces, and the leads and polynyas can appear either very bright (on the left of the image) or very dark (on the right). The tracks furthest to the right in the image show sigma 0 variations transverse to the tracks, with decreasing values away from the nadir, affecting both leads and floes.

https://doi.org/10.5194/egusphere-2026-2569
Preprint. Discussion started: 5 June 2026

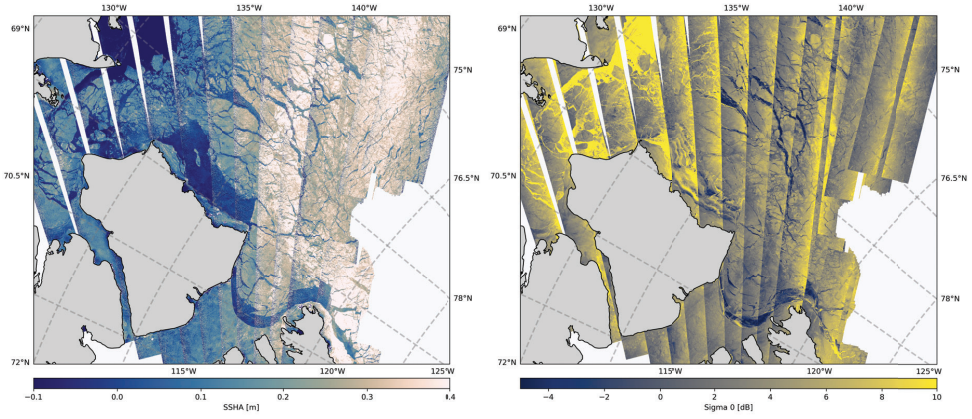

Figure 2. SSHA (left) and sigma 0 (right) from L3 LR 250m v2.0.1 product for all the SWOT ascending passes around Banks island from March 28th to April 10th 2024.

Each of these phenomena can be explained to a greater or lesser extent, but their variability from one pass to another is more surprising and requires more in-depth analysis in order to consider a systematic correction. The classification process, as well as any other type of sea ice measurement must therefore be robust to these variations. As we will see in the next section, this required the implementation of different types of pre-filtering of the SSHA and sigma 0 before the classification.

3 Sea ice classification methodology

3.1 Overview

As mentioned in the previous section, the lead / floe surface classification process is based on two parameters available in the L3 product: the SSHA and the sigma 0. After preprocessing the data, and using various filtering stages described below, multiple layers of bi-modal clustering are combined to provide a 4-value classification according to their agreements or disagreements. These values range from 0 to 3, which correspond to a definite floe and a definite lead, respectively. The intermediate values 1 and 2 are labeled as unsure floe and unsure lead.

Tracks are processed independently, one by one. The processing is done along the full track, above 50°N for the Arctic and below 50°S for the Antarctic, and where OSI SAF sea ice concentration is above 50%. The sigma 0 is logarithmically scaled and detrended cross-track wise, due to the near-nadir illumination, and henceforth named straightened sigma 0.

When computing over hundreds or thousands of passes along thousands of kilometers, several problems, related to physical and geometrical phenomena [JPL D-109532 (2025)] or processing effects, can be encountered, such as strong local sigma 0 illuminations, dark waters, remaining cross-calibration effects and miscellaneous artifacts. The used Mean Sea Surface (MSS)

https://doi.org/10.5194/egusphere-2026-2569
Preprint. Discussion started: 5 June 2026

is also not very suitable for the SWOT period because of the strong Dynamic Ocean Topography (DOT) over polar oceans [Veillard et al. (2024), Lin et al. (2023)]. Some of these issues (either acquisition or processing-related) can be observed in Figure 3. Much of the data processing in the surface classification process is implemented to mitigate these effects.

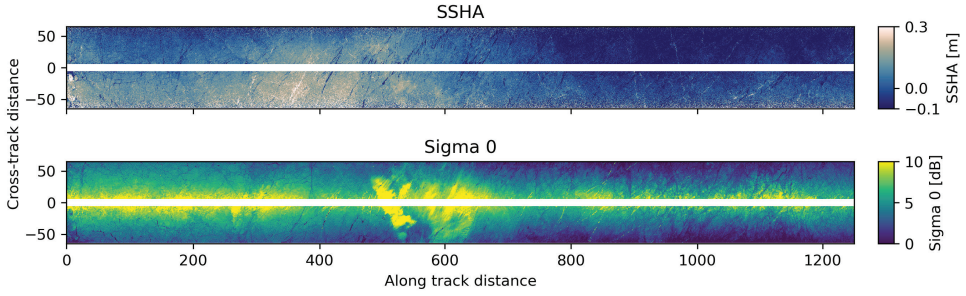

Figure 3. Illustration of the raw SSHA (top) and sigma 0 (bottom) for the pass 19 from cycle 13. The strong variability of the SSHA along track can be observed with, e.g., the drop in value on the right. The near-nadir sigma 0 illumination can also be seen, as well as a strong flash around 600 km from the origin.

One of the most important step of this processing is the removal of the low frequency in the data. This can attenuate the DOT, cross-calibration and illuminations variabilities to a great extent. This high-pass filtering is done on two different scales: one to compute the high-frequency of the data (both <40 km and <2 km), and the other to remove the trend in the data (>35 km across track, to deal with cross-calibration residues, and >50 km along track). However, removing the low frequency highlights the noise in the data, so a gaussian blurring is applied to this trend-corrected data to compensate for that (Sect. 3.2.1).

Filtering the low frequency of the data on the one hand, and keeping the preprocessed data on the other hand, leaves us with a combination of 5 parameters that can be used for the clustering:

- SSHA
- Straightened sigma 0
- High frequency SSHA (HF SSHA), <40 km and <2 km
- Absolute value of the high frequency straightened sigma 0 (HF sigma 0), <40 km and <2 km
- Trend-corrected SSHA

The combined use of high frequency and original data allows us to exploit different scales of the physical signal: while the original data provide an overview of the track and the true value of the measure, the high frequency data give a focused attention on elevation or backscatter local variations, thus discriminating leads from floes more efficiently. The absolute value

https://doi.org/10.5194/egusphere-2026-2569
Preprint. Discussion started: 5 June 2026

Intermediate classification 1	Intermediate classification 2	Intermediate classification 3
• HF SSHA	• HF SSHA	• HF SSHA
• HF sigma 0	• HF sigma 0	• HF sigma 0
• Straightened sigma 0		• Straightened sigma 0
• SSHA		• Trend-corrected SSHA

Table 1. Clustering input set variants for intermediate classifications 1, 2 and 3.

of the high frequency sigma 0 is used to match dark leads, or leads with low backscatter, as well as the more usual bright leads. From this combination of parameters we derive 3 clustering input sets variants, listed in Table 1.

From multiple qualitative and quantitative tests, we assessed that using the clustering on the first set of 4 parameters (set 1), mixing original and high frequency data, resulted in a more accurate surface classification than using only the high frequency data (set 2). However, due to the aforementioned issues in the data, this classification is occasionally misled by ambiguous data regions that lead to inconsistencies. This is mainly due to the length of the processed tracks, which can reach several thousands of kilometers and reveal variations of several tens of centimeters in the SSHA, either because of residual discrepancies of the MSS on ice-covered oceans, or because of natural large-scale variations, such as the Beaufort Gyre coupled with the lows off the Bering Strait [Veillard et al. (2024), Lin et al. (2023)]. The SSHA's sole criterion can then lead to false interpretations, such as attributing a hump to sea ice floes or a depression to polynyas. This is particularly the case off the Bering Strait. Similarly, the variability of sigma 0 along a track can also lead to this type of confusion. Despite the care taken with upstream processing, the flashes of strong sigma 0 mentioned above occur along the tracks over distances of up to several hundred kilometers (see Figure 3 for a visual example of this phenomenon).

The classification using the input set 3 benefits from the qualities of the two first input sets: it provides an accurate discrimination of leads and floes like the intermediate classification 1, while being almost as robust as the intermediate classification 2 method. However, despite the gaussian blurring to remove the noise, the classification on some passes is still noisy and sporadic leads appear in the middle of what is expected to be otherwise clean floes. The specific processing applied to these three intermediate variants is explained in Section 3.2.

In order to determine the relevance of each classification process according to the analysed track, we developed a quality check based on two criteria from the properties of the clustered data. The first one relies on the ratio of points classified as leads relatively to the total number of points, while the second one is based on the disparity of the data between two clusters. We use these tests to detect spurious intermediate classifications and to combine them to determine the best possible solution for the final result. The general development of the classification is summarized in Figure 5.

3.2 Implementation method

The principles of the method set out above are presented here step by step. These different stages are illustrated in Figure 5 for the general development, and in Figure 4 for details in the intermediate classification variants (with the same numbering as

https://doi.org/10.5194/egusphere-2026-2569
Preprint. Discussion started: 5 June 2026

inputs described in Table 1). Figure 5 is to be read from top to bottom. The arrows represent the data that is input at the top and sides of the boxes, and output at the bottom. The boxes are the processes operated on these data. These steps are described in more detail below. Fundamentally, this figure shows the transformation from the raw data, at the top, to one of the intermediate classifications (1, 2 or 3) at the bottom. On a higher level, Figure 5 shows how the data, and more particularly the intermediate classifications are handled to end up with the final 4-state consensus classification. The blue boxes in Figure 5 represent each of the processes from Figure 4.

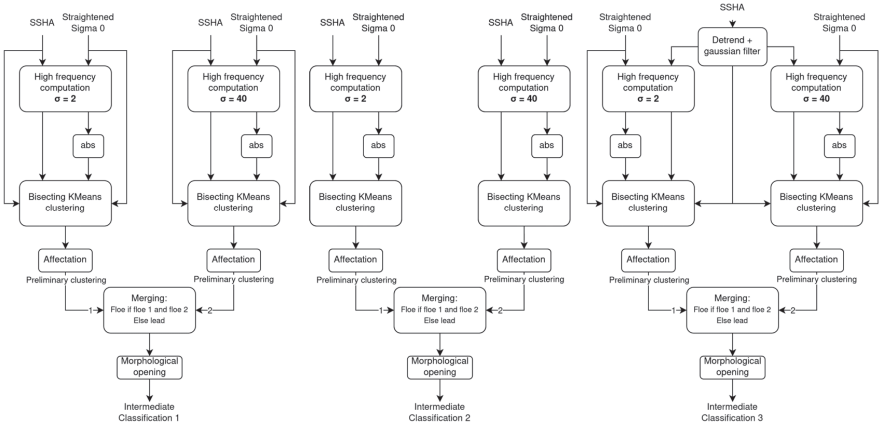

(a) Intermediate classification 1 **(b)** Intermediate classification 2 **(c)** Intermediate classification 3

Figure 4. Flowchart for intermediate classifications 1, 2 and 3. Intermediate classification 2 only feeds the high frequency into the KMeans clustering. Intermediate classification 3 detrends the SSHA before use. The rest is similar.

3.2.1 Intermediate classification

The intermediate classifications are the innermost part of the classification. They are applied multiple times during the classification of a single swath. They consist of three steps, each applied two times, and two more steps afterwards. The first three steps are the computation of the high frequency of the data (HF SSHA and HF straightened sigma 0), the clustering and the class affectation.

Computing the high frequency of the data is done using a gaussian filter. It is performed two separate times: one with σ=2 (<2 km) and one with σ=40 (<40 km). Those values were set from a visual identification of the best classification results on multiple sea ice scenes, and further tuning might be an area for improvement. The computations with the two kernels are done to ensure a good representation of differently sized floes: thin floes will appear better with a small kernel, but a larger kernel avoids creating "ice rivers" in the middle of large leads. For the clustering, the data are first scaled (μ=0, σ=1), then the proper

https://doi.org/10.5194/egusphere-2026-2569
Preprint. Discussion started: 5 June 2026

clustering algorithm is performed using an implementation of the Bisecting K-means algorithm with two target clusters (a constraint that can cause issues in high sea ice concentration scenes as discussed in Section 4). The clusters are then identified, with the leads cluster being the one with the lowest median SSHA of the two.

We then end up with two preliminary clusterings that are then merged into one: any point that is a lead in any of the two clusterings is classified as a lead, and only the floes that are classified as such in both classifications will end up as floes. After the two clusterings with the two kernels are merged, a binary opening is performed. It is used to remove isolated leads points that would otherwise appear in the middle of floes due to noise in the data or clustering inaccuracies. This step results in an intermediate classification, either 1, 2 or 3.

3.2.2 Suspected bad classification

Two tests were conducted to assess if an intermediate classification went wrong, as shown in Figure 5. The first one takes into account the fraction of leads, the second one considers the disparity between the two classes.

- Suspected too much leads: the intermediate classification is considered suspect if the pass has more than 80% of leads and enough points in the overall track.
- Suspected bad SSHA: using a linear discriminant analysis (LDA) model trained on manually assessed intermediate classifications, possible biases are found and the classification is consequently considered suspect if so. This model is based on 3 parameters from the data of the two (leads and floes) clusters: the absolute and relative difference of the median sigma 0, and the absolute difference of the standard deviation of the sigma 0.

3.2.3 Consensus classification process

This process is the outermost layer of the surface classification method, encompassing all the previous steps, as shown in Figure 5. It starts with a preprocessing of the data, removing open ocean areas in the pass and edited points (SSHA quality flag). The sigma 0 is logarithmically scaled and straightened, meaning that the median of every line across-track was removed from the data to reduce near-nadir illumination. Note that the HF sigma 0 is computed from this straightened sigma 0. Two simultaneous clustering processes then take place, as previously mentioned (the two lines in the process of Figure 5).

- On the one hand:
    1. The intermediate classification variant 3 is applied
- On the other hand:
    2. The intermediate classification variant 1 is applied
    3. If one of the two tests detect a suspect classification, the intermediate classification variant 2 is applied on the same dataset

https://doi.org/10.5194/egusphere-2026-2569
Preprint. Discussion started: 5 June 2026

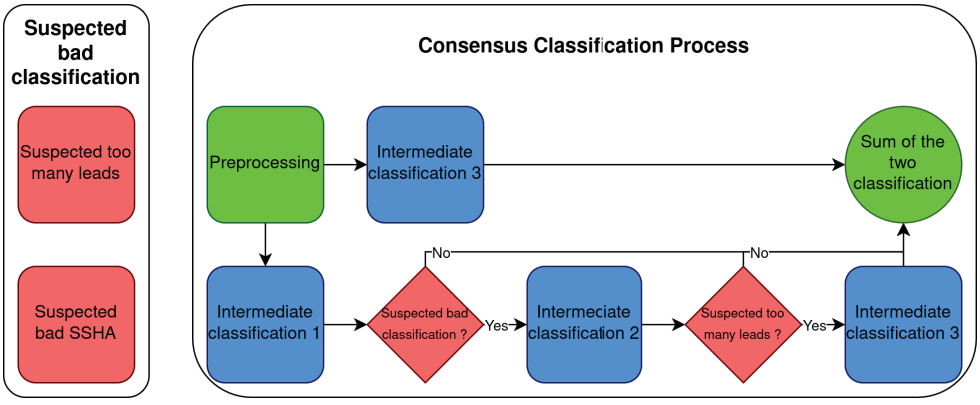

Figure 5. Sequence of processes to select the two best intermediate classifications. Depending on the results of the quality tests, pairs (3,1), (3,2) or (3,3) will be selected. Both intermediate classification 3 are distinct due to the random nature of K-Means clustering (see Section 3.2.1).

4. If the first test detects a suspect classification, the classification falls back on the intermediate classification variant 3

– Finally:

5. The two intermediate classifications are merged into the consensus classification

The merging of these two concurrent intermediate classifications allows for a better consideration of the complex states of the sea ice. The two intermediate classifications are merged as a 4-state final consensus surface classification. 0 is a certain floe, 1 and 2 are an unsure state, and 3 is a certain lead. It is constructed as follows: leads in both intermediate classification end up as leads; floes on both classifications end up as floes; results disagreeing in the two intermediate classifications are classified in the unsure middle state.

Appendix figure A1is an illustration of these processes, using the same layout as in Figure 4. For each step, from the raw data up to the intermediate classification 1, a slice in the swath was extracted and placed on the figure. Each small plot is then the input and output of the process boxes of Figures 4 and 5. Appendix figure A2 is an illustration of the processes using the layout of Figure 5, showing the final consensus classification. The two figures together demonstrate every step of the classification, here for a slice in the Northern Hemisphere of C13 T3.

https://doi.org/10.5194/egusphere-2026-2569
Preprint. Discussion started: 5 June 2026

Data type 1	Classification	Quality flag
lead	3	0
probable lead	2	18
probable floe	1	19
floe	0	20

Table 2. Quality flag values from the classification in the L3 LR 250m v2 product.

4 Results

The lead / floe surface classification is a 4-state classification computed at every point of the $250\,\mathrm{m}$ posting swath. It is stored in the SSHA quality flag parameter in the L3 LR 250m v2 product, with the particular values described in Table 2:

An illustration for multiple passes of the classification obtained is illustrated in Figure 8, right panel (see Sect. 5.1). The passes illustrated are the same passes as in Figure 2.

Appendix Figure A3 illustrates the crossing of the tracks 1 and 4 during the CalVal cycle 507 near Severnaya Zemlya in the Kara sea. The classification has been computed independently for the two tracks. Given the repetitiveness of the CalVal period with the 1-day cycle, crossovers have a low time delta. The classification should thus be similar at the crossover of tracks from a same cycle. This is what can be observed in Figure A3, which exhibits the self-consistency of the classification.

Finally, Figure 6 shows histograms of the SSHA for each of the 4 classes of the classification for the entirety of cycle 13. These distributions are consistent with an SSHA that is almost centred on zero for the leads, then its average value increases gradually with uncertain fractures, uncertain floes, and then floes, reaching an average of 20 cm.

This initial version of the classification, however, does not work equally well everywhere and at all times. Figure 7 illustrates the main limitations, with clear evidence of failure in front of the Bering Strait and some tracks across the Canadian Archipelago. In both cases, ice concentrations are significantly underestimated, but for different reasons.

The problem off Bering is due to a depression of more than $20\,\mathrm{cm}$ in the SSHA. As the classification is based on sigma 0 and the SSHA, this depression is interpreted as a large polynya. This depression is itself due to the MSS Hybrid [Laloue et al. (2025)] used in SWOT, which is not adapted to the SWOT period. In fact, this depression zone forms a dipole with the Beaufort Gyre, whose average annual sea levels have undergone considerable changes over the last 10 years, with a decrease of around $1\,\mathrm{cm/year}$ at the position of the depression and an increase of the same order at the position of the Gyre, i.e. a differential between the two poles of about $20\,\mathrm{cm}$ in 10 years [Veillard et al. (2024), Lin et al. (2023)]. The problem therefore probably stems from the fact that the MSS Hybrid constructed over the period 1993-2021 does not reflect this recent dynamic. We will see in the discussion section how this problem can be addressed in future version.

Classification failures in the Canadian Archipelago are of a different nature. They are due to the almost complete absence of leads, which prevents clustering from identifying two distinct classes, as only one is present. Fortunately, these cases are not too frequent and are easily identifiable, as we will see in the discussion section 6.

https://doi.org/10.5194/egusphere-2026-2569
Preprint. Discussion started: 5 June 2026

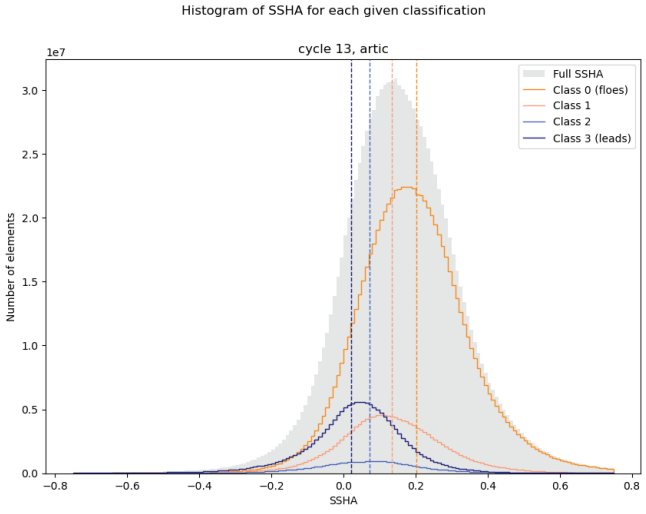

Figure 6. The histogram in grey is the SSHA distribution for each pixel of the Cycle 13 in the Arctic. It is redistributed by class according to the four coloured histograms, with leads in blue, floes in orange, and probable leads and probable floes in light blue and pink. The mean values of the SSHA, indicated by the vertical lines, are ordered as expected.

One final significant problem arises from the degradation of measurements on the inner and outer edges of the tracks over a width of approximately $10\,\mathrm{km}$ (i.e. a total of $40\,\mathrm{km}$). The tracks being processed and delivered in their entirety, these measurement noises substantially degrade the results. Here again, we have options for improving the processing, but we will see that only by excluding the borders of the classified tracks the overall results are significantly improved.

5 Assessments using other spatial observations

5.1 Comparison with MODIS

In order to assess the observation of small scale structures retrieved from the KaRIn sea ice classification algorithm, a comparison with an independent sensor is necessary. Such comparison is not straightforward as most of the reference products publicly available provide sea ice concentration information at a lower spatial resolution (e.g. OSI-408-d products from OSI SAF based on AMSR-2, the CMEMS Arctic sea ice products based on Sentinel-1 and AMSR-2, etc.). The MODIS sensors onboard the Terra and Aqua spacecrafts provide true color images (red, green, blue bands combination) at the spatial resolution of $250\,\mathrm{m}$, as for KaRIn LR Unsmoothed products (see Figure 8) and provide clear distinction between leads and floes surfaces in cloud free diurnal situations. Because MODIS has a viewing swath width of $2330\,\mathrm{km}$, several SWOT passes are needed to cover an

https://doi.org/10.5194/egusphere-2026-2569
Preprint. Discussion started: 5 June 2026

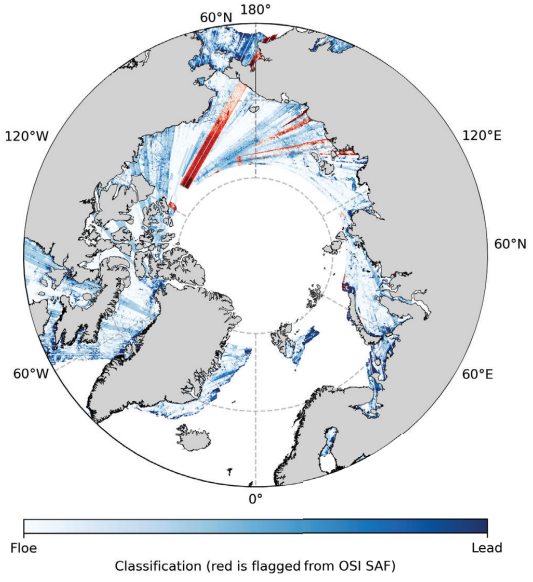

Figure 7. Example of classified ascending tracks during cycle 11. Classifications detected as inconsistent using OSI SAF are indicated in red (see Section 6.2). We can see they fail in the depression in front of the Bering Strait. The red track visible east of the antimeridian is a clear example of a failed classification due to the drop of SSHA in the region.

equivalent surface and visually compare the sea ice distribution. For this local comparison, illustrated in Figure 8, in the Kara sea, the SWOT sea ice classification (right panel) is retrieved from ascending passes covering the area from March 28th to April 10th 2024. The MODIS image, displayed on the right panel, was acquired on April 4th. At first glance, there is, visually, a good spatial correlation between the blue areas from SWOT classification and the darker regions from the MODIS image. These features correspond to surfaces identified as leads, and the overall agreement between the two observation sources over this local area highlights the capabilities to retrieve sea ice surface type from KaRIn measurements at small scales.

5.2 Comparison with ICESat-2 and Sentinel-3

In this section we compare the KaRIn surface classification to that of the laser altimeter ICESat-2 and the nadir Ku altimeter Sentinel-3. First we present the methodology used to perform the comparisons, which is common to ICESat-2 and Sentinel-3, and then we present the results for each satellite separately.

https://doi.org/10.5194/egusphere-2026-2569
Preprint. Discussion started: 5 June 2026

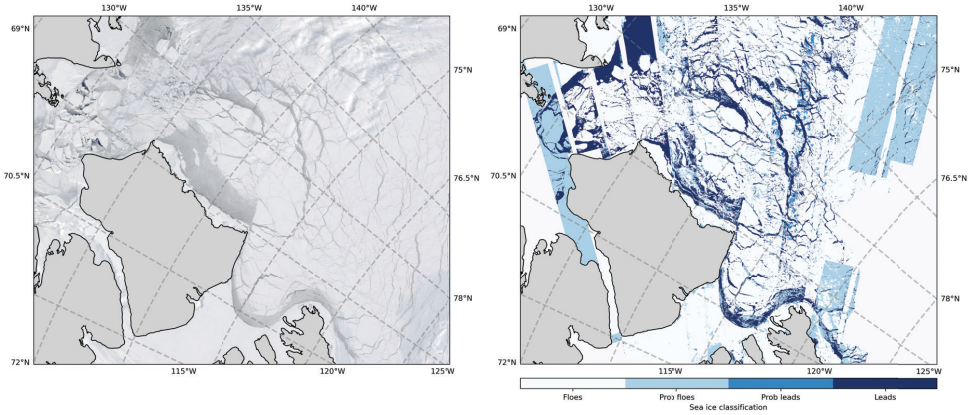

Figure 8. Left panel: true color image from the MODIS instrument acquired on 4th April 2024. Right panel: sea ice classification from KaRIn measurements: leads in dark blue, floes in white, unsure in intermediate blues. In this local illustration west of Banks island, SWOT ascending passes were selected from March 28th to April 10th 2024.

5.2.1 Methodology

The analyses are performed on crossing points computed for absolute latitudes beyond 65°, at least $60\,\mathrm{km}$ away from the shore, and with a maximum time-lag of $15\,\mathrm{min}$. Such a time-lag should minimize the effects of sea ice drift that can impact the comparison between the observations. Indeed, ice drifts up to $1\,\mathrm{km\,h^{-1}}$ [Tschudi et al. (2019)] result in displacements of less than $250\,\mathrm{m}$ in $15\,\mathrm{min}$, which corresponds to the posting of the KaRIn data. Based on the SWOT Science phase data for winter 2023/2024, we find 18 usable crossing points in the Antarctic (August to October) and 38 in the Arctic (November to May) for ICESat-2. For Sentinel-3 we obtain 135 usable crossing points in the Arctic, for the same period. We do not extend the analysis to the South Pole as we consider the 135 cases as enough for a first robust analysis. More crossing points are found but discarded due to the absence of leads or of data altogether, from ICESat-2/Sentinel-3 or KaRIn datasets. Note that we do not consider cases where more than 50% of KaRIn's measurements, along the altimeter's track, are classified as unsure lead/floe to exclude complex cases where the classification is less certain.

For each crossing point case, the correspondence between the ICESat-2/Sentinel-3 altimeter and the KaRIn swath measurements is computed using a python library for optimized interpolation[1]. This routine yields the distance between each altimeter measurement and the closest KaRIn pixel. Given the along-track resolution of Sentinel-3 of about $300\,\mathrm{m}$ (Section 5.2.3), at most two measurements are found within a KaRIn $250\,\mathrm{m}$-side square pixel, i.e. up to $176\,\mathrm{m}$ from its center. We take the closest one and its corresponding surface classification. As for ICESat-2, owing to its finer along-track resolution of a few tens of meters (Section 5.2.2), the number of measurements within a KaRIn pixel can go up to 40-50, depending on the relative ori-

[1] https://github.com/CNES/pangeo-pyinterp

https://doi.org/10.5194/egusphere-2026-2569
Preprint. Discussion started: 5 June 2026

entation altimeter track vs swath. Here we consider that ICESat-2 detects a lead over a given KaRIn pixel if at least one of the multiple measurements within that pixel is a lead[2], otherwise the associated surface classification is floe. Note that ICESat-2's leads are of different types according to their properties (2 to 9, see Section 5.2.2 for more details). To retrieve that information, we take the mode of the leads type of the valid measurements within each pixel.

Having the correspondence between the altimeter and the swath measurements, we can perform a point-by-point quantitative comparison. For that we make use of the phi coefficient, also called Matthews correlation coefficient (Matthews 1975), which is a measure of association for two binary variables and particularly suited in the case of non-similar populations. This is the case here, where the proportion of leads is generally much lower than that of floes. The phi coefficient ranges from +1 for a perfect agreement to -1 for a perfect disagreement, where 0 means no association. Longépé et al. (2019) use this indicator in a similar study, to assess the sea ice lead detection on Sentinel-1 images and collocated Sentinel-3 altimetry data, and obtain values around 0.2-0.3.

In the following we present the results for the comparisons between KaRIn and the two altimeters.

5.2.2 ICESat-2

The photon-counting lidar altimeter on-board ICESat-2, ATLAS, transmits pulses split into six beams (three strong and three weak) whose individual footprints of about $11\,\mathrm{m}$ are separated by $0.7\,\mathrm{m}$ along-track (Neumann et al. 2019). Here we use ATL10 v006 data, in which the surface height is provided for each beam at a lower and variable along-track resolution ($7\,\mathrm{m}$ to $200\,\mathrm{m}$), as it is estimated from the distribution of about 150 signal photons, cumulated over variable distances depending on the surface and on the beam. Based on the height distribution but also on background noise and error measure, a surface type is assigned to each measurement (Kwok et al. ATBD 2022). We follow the same approach as Kwok et al. (ATBD), namely by considering only the specular types 2 to 5 as leads (but without threshold on the height) and type 1 as floes. Furthermore, we consider only the middle strong beam in the current analysis (Kwok et al. 2021, Bagnardi et al. 2021).

Figure 9 shows the resulting surface classification from ICESat-2 overlaid on that of KaRIn for two crossing points, one in the North Pole on 12/04/2024 and one in the South Pole on 30/08/2023. The first region lies close to the Alaskan coast, where polynia form regularly due to strong offshore north-eastern winds (Cape Bathurst, Preußer et al. 2019). The second region, over the Riiser-Larsen sea, presents both thin leads within fractured ice as well as larger lead openings. Visually the two solutions seem to agree rather well, which is confirmed by the phi coefficients of 0.50 and 0.57 respectively, translating the strong correspondence between KaRIn and ICESat-2 for these two cases. When considering all 38/18 crossing points in the North/South Pole together, we obtain a phi coefficient of 0.17/0.34. There is hence a global moderate agreement in the South Pole and a weaker agreement in the North Pole, for the cases considered (Sect. 6) When looking at each case processed

[2]Compared to swath altimetry, nadir altimetry is more sensitive to the lead's orientation with relation to the along-track direction. This is particularly the case for the high-resolution ICESat-2 altimeter. To illustrate our choice, one could imagine for instance, a thin lead that crosses a KaRIn pixel and that is roughly perpendicular to ICESat-2's track. It will be thus only detected by a few measurements by the nadir laser altimeter. In any case, to confirm this choice we ran the analysis for different minimum proportions, from 0 to 50% every 5%, of leads identified by ICESat-2 within a KaRIn pixel. We found that the lowest percentage of 0% used here, which corresponds to assigning a lead if there is at least one lead detected yields the best agreement with KaRIn.

https://doi.org/10.5194/egusphere-2026-2569
Preprint. Discussion started: 5 June 2026

individually, we find that the lowest phi coefficients occur when only a few leads are detected: if these few leads are not perfectly aligned between the two observations, the phi coefficient drops even if the accordance over (the prevailing population of) floes is good. Given that the time-lag of 15 min between the two acquisitions should minimize the effects of ice drift, as mentioned above, the misalignment is therefore most certainly due to different responses by the two sensors to the surface, combined with the assumptions taken here to conciliate the difference in ground resolutions.

We use the ICESat-2 classification along each track to compute a sea ice concentration, SIC = total_nb_floes/total_nb_measures, for each case and find that the phi coefficient is anticorrelated with the SIC (Pearson correlation coefficients of -0.35 and -0.57 for the North and South Poles, respectively): the results improve with the number of leads. In the Arctic the phi coefficient increases significantly in April and May, with a mean of 0.34 for their 13 cases, which can be partly explained by the lower SIC, thus higher fraction of leads, for these months (91% versus 95% for the rest of the period).

The analyses presented in this section give a first and good assessment of KaRIn's surface classification with relation to ICESat-2, despite the limited number of crossing points. Future work will extend this analysis to a larger period and investigate the surface classes not considered here. Note that we repeated the quantitative analysis by including ICESat-2 dark leads (types 6 to 9) and obtained phi coefficients that are degraded by about 30% for both hemispheres. Further investigation should also consider the unsure surface types detected by KaRIn (Sect. 6). The left panel of Figure 9 illustrates the complexity of the surface classification on a region with polynia: recently formed ice over this area of open water results in a variable classification by the two sensors.

We note that the potential of KaRIn for sea ice studies was also recently illustrated by Kacimi et al. (2025) and Müller et al. (2026), by comparing with ICESat-2 observations. Both works analyzed the difference in height between the two sensors, finding a similar mean standard deviation of 8 cm. The mean difference in height estimated by Kacimi et al. (2025) for their 2 cases is less than 2 cm, whereas Müller et al. (2026) find higher values, up to tens of centimeters, for the 550 crossovers analyzed. Their results presumably translate the current limitations of the calibration applied to the data version used in the study. Fischer et al. (2025) also combined KaRIn and ICESat-2 over the Beaufort Sea, showing an excellent agreement in topography over leads and undeformed ice on spatial scales of 0.5 to 50 km. They demonstrate the power of KaRIn in detecting km-sized ice structures of a meter height, that are unseen by the much higher resolution ICESat-2 altimeter. The authors also used the current sea surface classification in their local analysis, finding that both leads and deformed ice are successfully detected by KaRIn, though some less rough sea ice was mistakenly classified as open ocean.

5.2.3 Sentinel-3

The nadir altimeter Sentinel-3 operates in SAR mode with an along-track footprint of ~330 m and an across-track footprint of ~7 km. Here we consider only the "surface_type_classification_20_ku" variable from the official Sentinel-3 sea ice thematic products, a flag that uses a combination of thresholds applied to both the peakiness of the SAR waveform and the sea-ice concentration from auxiliary data. An "unclassified" category also exists in the case of measurements detected as ambiguous (Aublanc et al, 2025).

https://doi.org/10.5194/egusphere-2026-2569
Preprint. Discussion started: 5 June 2026

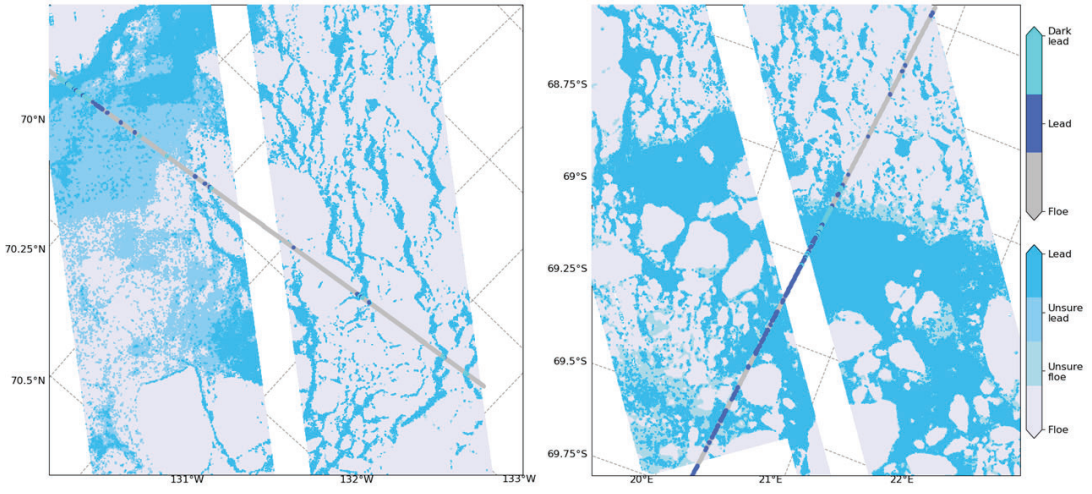

Figure 9. KaRIn and ICESat-2 surface classification at two crossing points: (a) SWOT cycle 13 track 431, 00h29m 12/04/2024, time-lag of 10.5 min, in the Arctic and (b) SWOT cycle 2 track 544, 12h44m 30/08/2023, time-lag of 7.2 min, in the Antarctic. We show the ICESat-2 classification over each KaRIn pixel, obtained as described in the text. Even though not considered in the analysis, the ICESat-2 dark leads (see top colour bar) and unsure lead/floe KaRIn classes (see bottom colour bar) are also displayed. The phi coefficient, quantifying the agreement between two classifications, is 0.5 for (a) and 0.57 for (b).

The phi coefficient derived for the 135 identified crossing points is 0.24. There is hence a moderate agreement between Sentinel-3 and KaRIn, which is nevertheless better than that observed with ICESat-2 in the North Pole, if we consider its lower phi coefficient of 0.17 (section 5.2.2). This could be explained by the number of crossing points analysed (135 w.r.t 38) or by a real difference pertaining to the different sensors onboard Sentinel-3 and ICESat-2. Figure 10 presents the surface classification results from Sentinel-3 and SWOT over two crossing points in the North Pole in Spring 2024, observed on 30 March 2024 and 14 April 2024. Figures 10a and Figure 10b correspond to a case with a majority of sea ice interspersed with several leads. Visually, the two sensors seem to agree well, as every lead identified by the SWOT classification also corresponds to points classified as lead by Sentinel-3. Similarly, the majority of the points identified as ice floes by SWOT are also identified as floes by Sentinel-3, with a few "unclassified" points. However, Sentinel-3 detects several leads near 76.8°N that are classified as ice floes by SWOT. Upon examination of the corresponding KaRIn sigma 0 values (Figure 10a), these points exhibit characteristics consistent with leads, albeit with lower sigma 0 values with respect to the surrounding ice floes. This pattern is typical of dark

https://doi.org/10.5194/egusphere-2026-2569
Preprint. Discussion started: 5 June 2026

leads (Section 2.2), which are commonly misidentified as ice floes by SWOT due to their low sigma 0 values. Interestingly, for this particular feature, some points are labeled as “unsure floe”, suggesting that the classifier partially recognized the presence of leads (see Section 6).

Figures 10c and 10d present an example featuring more fractured ice, characterized by large leads. Two distinct regions are observed: the left side of the image appears to be dominated by small ice floes and dark leads, associated with low-contrast backscatter values (KaRIn sigma 0, Figure 10c). In this complex zone, Sentinel-3 struggles to reliably distinguish between leads and floes that are often mixed in the footprint, resulting in a combination of floes, leads, and unclassified points. The SWOT classification also encounters difficulty in this area, predominantly classifying it as ice floes, with some points labeled as leads or "unsure floe." Although the SWOT classifier does not consistently detect the darker leads, it is noteworthy that it successfully identifies some of them. In contrast, the right side of the image displays a markedly higher roughness contrast, with bright leads and a large ice floe clearly identified. Both SWOT and Sentinel-3 accurately classify these features, showing strong consistency between the two sensors. Overall, in this challenging case, the SWOT classification demonstrates robust performance given the surface complexity.

When analysing each of the 134 crossing points individually, we find that 33% of the cases have a phi coefficient above 0.3, which indicates moderate agreement. It is noteworthy that the months of April and May yield the highest phi coefficient values with 0.34 for 49 cases, which is comparable to the value obtained in the same period with ICESat-2 (see Section 5.2.2). This could be explained by the higher number of leads observed during this period, which helps the classification. Among smaller phi coefficient cases ($\phi < 0.2$), we find that a large portion corresponds to regions where KaRIn sees the leads as “darker” than the sea ice, as displayed in Figure 10a and Figure 10b. As explained above, for these cases the sea ice classification algorithm might have some issue disentangling the two populations (see Sect. 6), resulting in a suboptimal classification and hence, a poorer agreement with Sentinel-3’s sensor that is not impacted by this issue. However, as observed in Figure 10, these leads are sometimes identified as “unsure lead” or “unsure floes”, showing that using all the outputs from the classifier may improve the leads/floes detection.

The analyses presented in this section give a first assessment of KaRIn’s surface classification with relation to Sentinel-3, showing an overall good agreement. Future work will extend this analysis to the South Pole, and for a longer period.

5.2.4 Assessment using OSI SAF/AMSR-2 sea ice concentration

The classification provides information both on the scale of a floe and on the scale of an entire hemisphere. By binning the data, here on a $12.5\,\mathrm{km}$ grid, a map of the sea ice concentration is generated. Figure 11 shows the sea ice concentration from April 2024, computed as such:

$SIC = \frac{n_0}{n_0+n_3}$

with n_0 and n_3 being the number of points in the classes 0 and 3 for each bin. The influence of classes 1 and 2 on the sea ice concentration is not explored here. A visual assessment of the map in Figure 11 establishes the good quality of the classification, as very few artifacts of passes or binning boxes appear. Some structures are also consistent on the large scales:

https://doi.org/10.5194/egusphere-2026-2569
Preprint. Discussion started: 5 June 2026

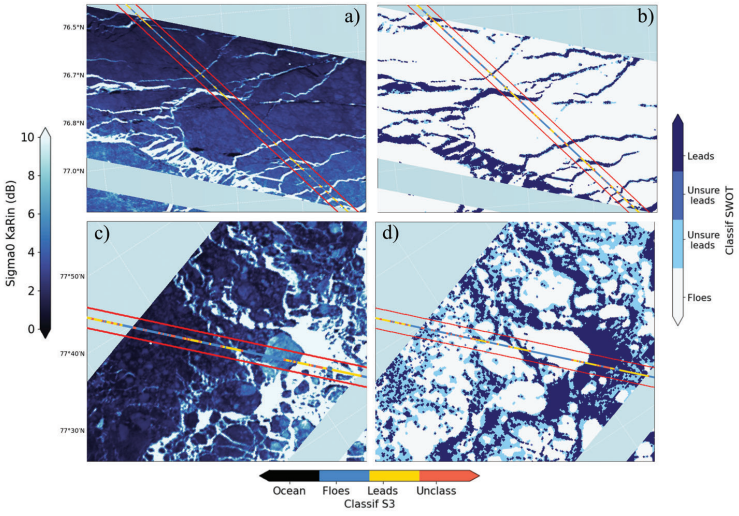

Figure 10. SWOT sea-ice classification compared to the Sentinel-3 surface classification for two crossing points with the associated SWOT sigma 0: top plots (a)(b) are for SWOT cycle 13 track 496, 07h02m 14/04/2024, time-lag of 1 min 43 s; bottom plots (c)(d) are for SWOT cycle 13 track 87, 17h09m 30/03/2024, time-lag of 14 min 46 s. Both regions are in the Arctic. The left panels (a)(c) correspond to the KaRIn sigma 0 and the right panels (b)(d) to the KaRIn sea ice classification. The red lines represent the Sentinel-3 across-track resolution. The phi coefficient, quantifying the agreement between the two classifications, is 0.35 for (a)(b) and 0.58 for (c)(d), respectively.

fractures appear on the northern coast of Russia, in the Laptev and East Siberian seas, or near Canada in the Beaufort sea. It is possible to see polynyas below the wind of the islands in the Kara sea.

Nevertheless, as it has been shown previously, the along-track classification is not working as well for all the seasons. This can be clearly observed with the 12 monthly maps for 2024 shown in Appendix Figure A5. In the following section, we present recommendations to limit these issues, as well as the approaches we are considering to correct or mitigate them in future versions.

6 Limitations, Recommendations and Evolutions

6.1 Known limitations

This work has resulted in the production of a first classification of sea ice that already allows to select SWOT measurements above open water or above ice floes. However, this initial version has a number of identified limitations.

https://doi.org/10.5194/egusphere-2026-2569
Preprint. Discussion started: 5 June 2026

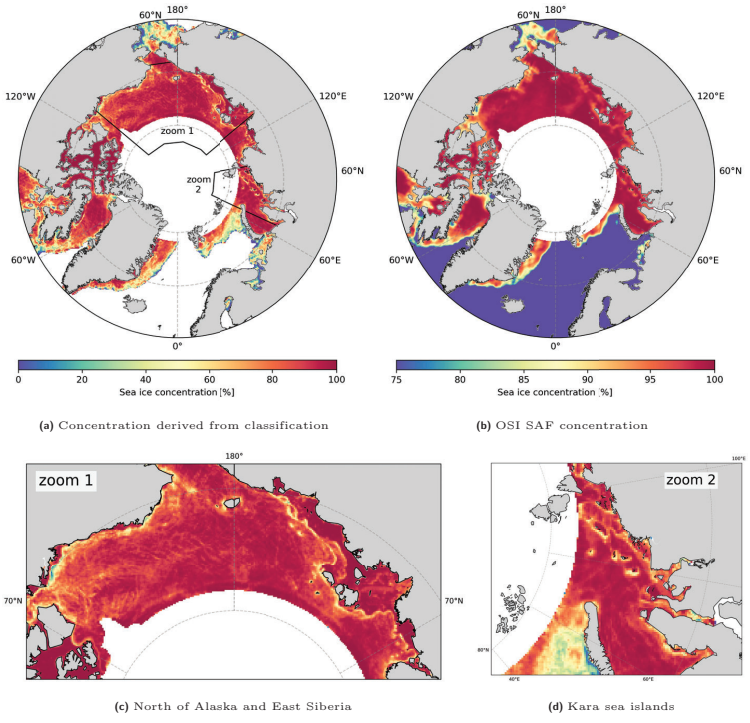

(a) Concentration derived from classification

(b) OSI SAF concentration

(c) North of Alaska and East Siberia

(d) Kara sea islands

Figure 11. Sea ice concentration for April 2024 computed from SWOT classification (top left) and produced by OSI SAF from AMSR-2 (top right, OSI-408a, April 15th). OSI SAF concentration is ranged from 75% to 100% to show more contrast in ice-covered areas. The zooms below from the SWOT concentration map allow us to observe the large polynyas along the coasts and even the West drift of the sea ice from Banks Island due to Beaufort Gyre (left zoom) and the polynyas below the wind of the small islands East of Kara Sea (right zoom).

Two of these limitations are minor issues that will be resolved in the next release. These are the limitation of processing to latitudes above 60° N/S, and the loss of a small area in the Arctic west of Prince Patrick Island between longitudes 123°W and 134°W and above latitude 75.5°N. They are both due to missing auxiliary data that have been identified and solved internally.

415 The other limitations were mainly presented in the results section 4. They cause failures across the entire track or portions of tracks. Fortunately, the failures are limited to about 10% of the tracks. The recommendations presented here allow these cases to be filtered out. We will then discuss the actions we plan to take to correct or mitigate these issues in future versions.

https://doi.org/10.5194/egusphere-2026-2569
Preprint. Discussion started: 5 June 2026

6.2 Usage recommendations

In order to limit measurement noise, we recommend excluding the $10\,\mathrm{km}$ bands on the inner and outer sides of both swaths, i.e. keeping the only data that is between $10\,\mathrm{km}$ and $60\,\mathrm{km}$ from the nadir (compared to the full swath distance that ranges from $5.5\,\mathrm{km}$ to $65\,\mathrm{km}$ from the nadir). An even stricter restriction, consisting of retaining only data between $15\,\mathrm{km}$ and $55\,\mathrm{km}$, will further improve the results, but this must be weighed against the loss of coverage. These restrictions will likely be eased in the future as treatments and classification improve.

The current classification largely underestimates the concentration. We do not have yet fully analysed the two unsure flags (values 1 and 2) but the flag 'unsure floes' are essentially floes, and according to the application (e.g., computation of the concentration), can be considered as such. We have observed that the unsure leads are often a very new and thin layer of ice, probably at the water level. Here again their usage will depend on the application.

Failed tracks or portions of tracks can also be identified and excluded using concentration information from OSI SAF, available in SWOT's L3 Unsmoothed product in the variable 'cvl_ice_conc'. This OSI SAF parameter has a native resolution of around $10\,\mathrm{km}$ and is not very sensitive to small variations in concentration. The orders of magnitude are, however, correct. By recalculating the concentration of sea ice from the classification, we can thus ensure that the concentration we obtain is consistent with OSI SAF. This calculation is easily done by aggregating the $250\,\mathrm{m}$ points into regions of $32.5\,\mathrm{km} \times 50\,\mathrm{km}$, which corresponds to 4 regions across-track (2 on each swath) to account for a bigger variation in this direction. The ratio of floes, unsure floes and unsure leads to the total valid points is then calculated for each of these regions. If the mean difference between the classification and OSI SAF of these ratios in all regions of a single SWOT track is above a threshold (we here chose 30%), the track or the portion of track should be considered as failed.

6.3 Planned evolutions

There are multiple changes we plan on making to improve the classification and its ease of use.

The first change we propose is to add a classification quality flag based on comparison with the OSI SAF concentration as described in the section above (Sect. 6.2).

The main causes of classification failures fall into two broad categories: 1) variability in SSHA along tracks, mainly due to MSS no longer corresponding to the average sea level over the SWOT period, 2) insufficient number of fractures in the ice pack to determine sea level and identify two distinct classes. While there are other elements than can explain failures, they are either measurement related or harder to interpret, and thus more difficult to fix.

For the first case, we have identified two procedures that largely attenuate the issue. The first procedure consists in zeroing out the variability of the mean sea level over the SWOT period, or more precisely, a "correction" of the MSS by calculating the DOT relative to the MSS for the year 2024 (Appendix figure A4). This involves calculating the average SSHA across all leads identified with SWOT during 2024. The DOT2024 is then subtracted from the SSHA across all tracks. This technique significantly improves the results, but it can also introduce bias if in certain regions ice floes are systematically classified as leads. It is therefore important not to include leads in areas that do not meet the quality flag.

https://doi.org/10.5194/egusphere-2026-2569
Preprint. Discussion started: 5 June 2026

The second approach is similar, except that the SSHA is re-interpolated on each track, again relying solely on reliable leads and in areas that meet the quality flag. This approach also has the benefit of correcting better the potential remaining cross-calibration issues.

These two approaches can be combined, and initial results show very significant improvements (Appendix figure A5). However, this requires more complex processing as it involves several iterations of classification: a first iteration to identify reliable leads, then a second iteration, after correcting the SSHA, to take full advantage of it. We are therefore also working on optimising the data processing.

There are also small improvements in the data pre-processing we are looking into, notably a better near-nadir illumination correction for the sigma 0 and a clustering trained without the swath edges to avoid bad data.

Looking ahead, we are also considering the possibility of using this initial classification to implement machine learning models that could incorporate other parameters, such as the consistency of measurements or the viewing angle of the points considered (lateral position in the track).

L3 LR Unsmoothed v3 product that will be released during the first semester of 2026 will include 3 different sea ice classification products from 3 different methodologies :

- One is a slight improvement of the classification described in this paper with some of the optimizations mentioned in this chapter.
- Another is a classification based on the XGBoost machine learning algorithm trained on the best tracks from this paper's classification during the CalVal period.
- The third one is a classification based on an iterative process using Markov chain partitioning.

These different solutions may help in determining the best methodologies for sea ice classification.

7 Conclusions and Perspectives

This article presented the methodology used to produce an initial solution for classifying sea ice between SWOT measurements covering ice and those covering open water in leads or polynyas. Ambiguous cases are grouped into two other categories: unsure leads and unsure floes. The latter are essentially floes, while unsure leads may include thin ice or floes in complex structures. The latter still needs to be analyzed in greater detail.

This initial classification was evaluated against MODIS images and classifications from the Sentinel-3 and ICESat-2 nadir altimeters. Comparisons with MODIS show that large ice structures and fractures are well observed with the SWOT classification. The correspondences with nadir altimeters are correct without being extraordinary, highlighting the difficulty of making small-scale comparisons of a dynamic surface with non-synchronous data and without indisputable reference data.

The classification was also used to estimate monthly sea ice concentrations on $12.5\,\mathrm{km} \times 12.5\,\mathrm{km}$ grids and evaluate them in relation to the OSI SAF 408a product. The results show that SWOT allows to perceive much more fine structures than OSI SAF,

https://doi.org/10.5194/egusphere-2026-2569
Preprint. Discussion started: 5 June 2026

which explains the lower sea ice concentration obtained with SWOT. However it is most probable that this classification aims to an underestimation of the concentration.

However, we propose strategies for filtering out the least reliable classifications and have shown that this strategy makes it possible to obtain very realistic concentration maps. We have also presented various avenues for improving this classification in a future version.

This classification and its future developments are already opening up possibilities for extending SSHA measurements to ice-covered oceans and for measuring the freeboard height of sea ice, a prerequisite for determining sea ice thickness.

Data availability. The data are available from AVISO https://www.aviso.altimetry.fr/en/index.php?id=5483

Author contributions. GJ: Methodology, Software, Validation, Visualization, Writing.
SF: Coordination, Methodology, Writing.
MR: Coordination, Methodology, Writing.
FP: Validation, Software, Visualization, Writing.
MA: Validation, Software, Visualization, Writing.
AT: Software, Validation, (review)
IB: Software, Validation, (review)
LY: Coordination, Methodology, (review)
RC: Software, Production launch
GD: Coordination, (review and editing)

Competing interests. The authors declare that they have no competing interest.

Acknowledgements. The authors acknowledge ESA/CROPS and CNES/SPIceSea projects for their support of this study.

https://doi.org/10.5194/egusphere-2026-2569
Preprint. Discussion started: 5 June 2026

Appendix A: Appendix Figures

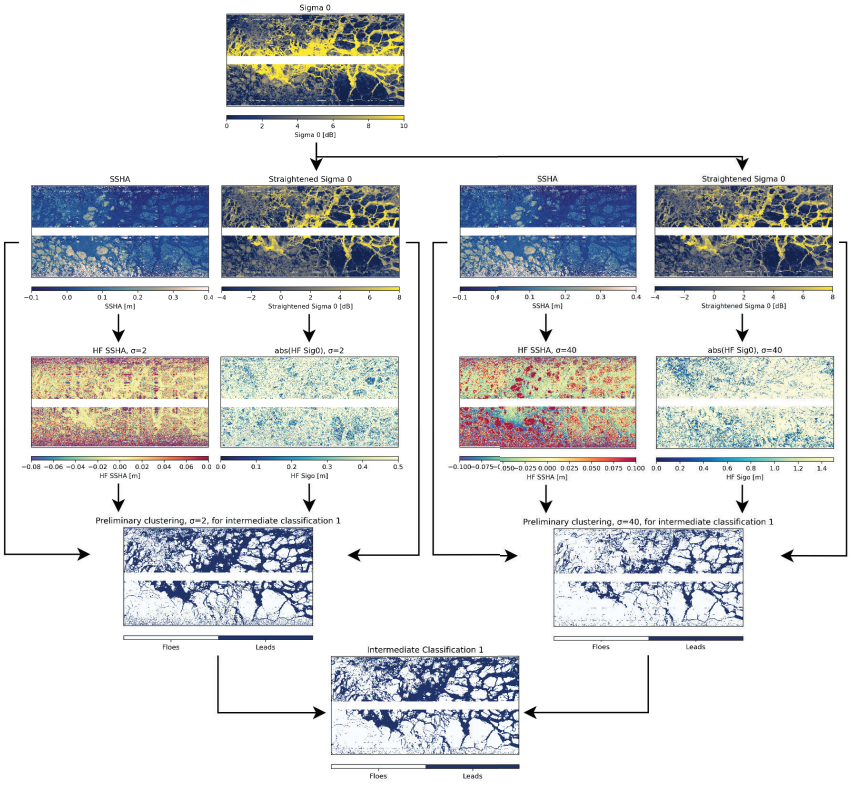

Figure A1. Illustration of a slice of SWOT track showing the different steps in the intermediate classification process.

https://doi.org/10.5194/egusphere-2026-2569
Preprint. Discussion started: 5 June 2026

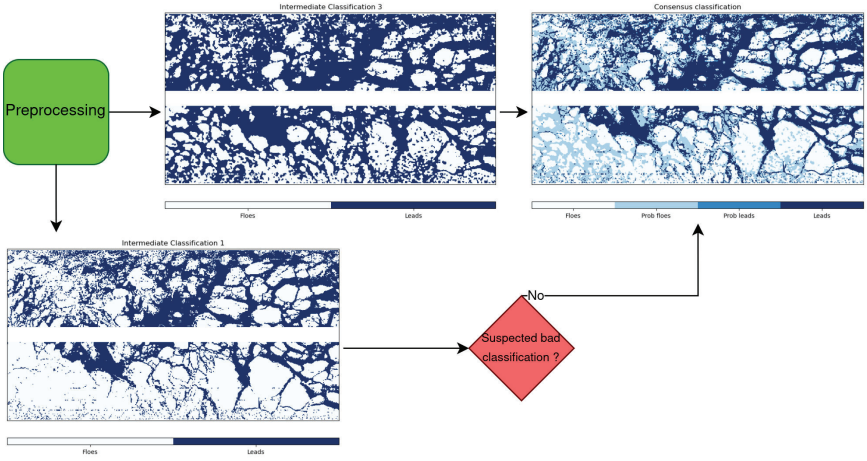

Figure A2. Illustration of the merging of two intermediate classifications to form the consensus classification.

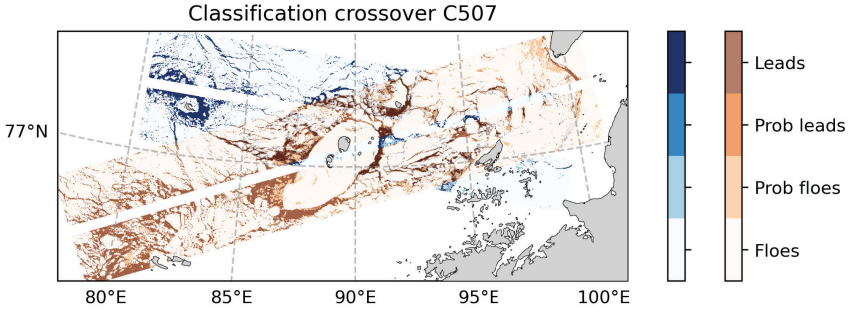

Figure A3. Classification for the crossover of passes C507 T1 and C507 T4 during the Calval phase, on April 30th 2023, with a time delta of 1 hour 45 minutes.

https://doi.org/10.5194/egusphere-2026-2569
Preprint. Discussion started: 5 June 2026

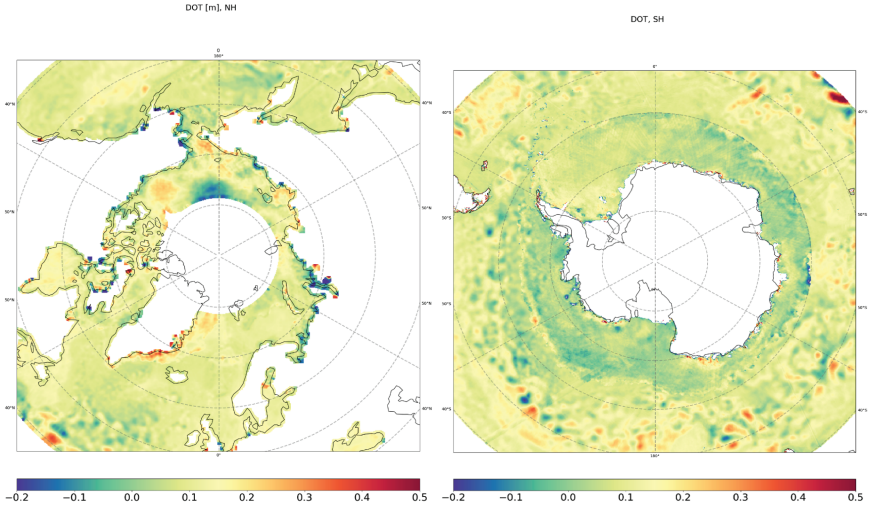

Figure A4. Dynamic ocean topography 2024 computed as the mean of the SSHA for all leads seen by SWOT during this year.

https://doi.org/10.5194/egusphere-2026-2569
Preprint. Discussion started: 5 June 2026

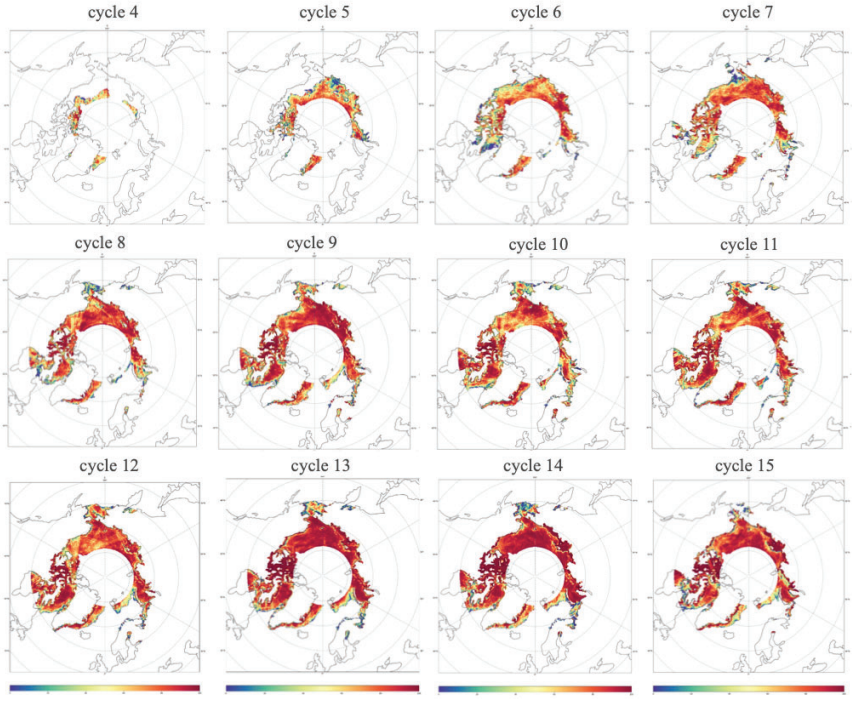

Figure A5. Sea ice concentration based on the classification in the L3 unsmoothed product for cycles 4 to 15 (Sept. 2023 to May 2024) without filtering.

https://doi.org/10.5194/egusphere-2026-2569
Preprint. Discussion started: 5 June 2026

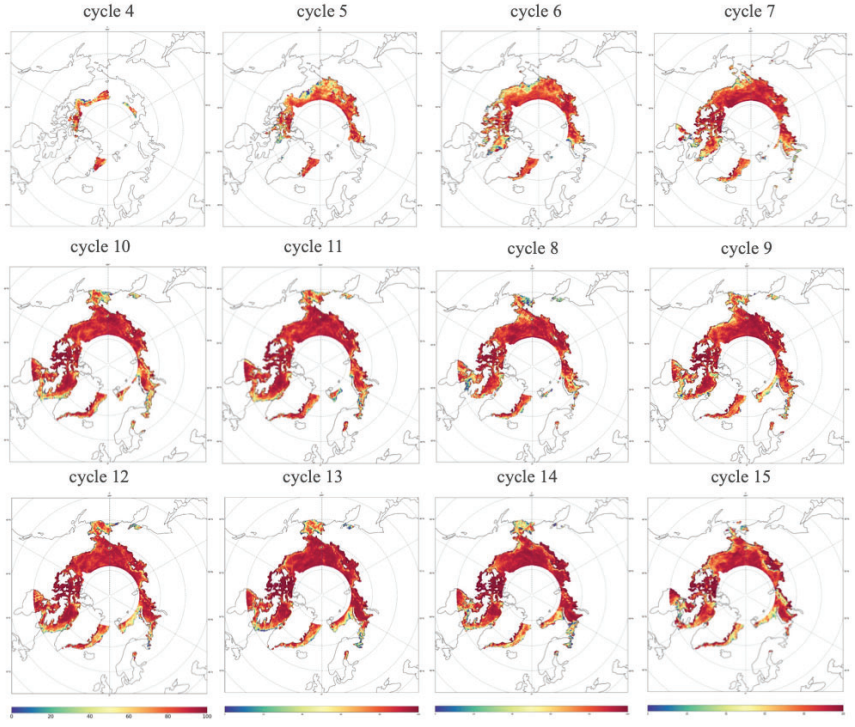

Figure A6. Sea ice concentration based on the classification in the L3 unsmoothed product for cycles 4 to 15 (Sept. 2023 to May 2024) with filtering following recommendations in section 6.

https://doi.org/10.5194/egusphere-2026-2569
Preprint. Discussion started: 5 June 2026

References

AVISO: DUACS Level-3 SWOT KaRIn (L3_LR_SSH) User Handbook, AVISO, CNES,CLS, https://doi.org/10.24400/527896/A01-2024.003, 2024.

Dibarboure, G., Ubelmann, C., Flamant, B., Briol, F., Peral, E., Bracher, G., Vergara, O., Faugère, Y., Soulat, F., and Picot, N.: Data-Driven Calibration Algorithm and Pre-Launch Performance Simulations for the SWOT Mission, Remote Sensing, 14, https://doi.org/10.3390/rs14236070, 2022.

Dinardo, S., Maraldi, C., Cadier, E., Rieu, P., Aublanc, J., Guerou, A., Boy, F., Moreau, T., Picot, N., and Scharroo, R.: Sentinel-6 MF Poseidon-4 radar altimeter: Main scientific results from S6PP LRM and UF-SAR chains in the first year of the mission, Advances in Space Research, 73, 337–375, https://doi.org/https://doi.org/10.1016/j.asr.2023.07.030, 2024.

Fischer, R., Farrell, Sinead, L., and Duncan, K. e. a.: Swath Mapping Altimetry over Sea Ice: First Results from the Surface Water and Ocean Topography (SWOT) Mission., ESS Open Archive, https://doi.org/10.22541/essoar.174619911.18378288/v1, 2025.

Jiang, M., Xu, K., and Wang, J.: Evaluation of Sentinel-6 Altimetry Data over Ocean, Remote Sensing, 15, https://doi.org/10.3390/rs15010012, 2023.

JPL D-109532: Revision A, "SWOT Science Data Products User Handbook," Jet Propulsion Laboratory Internal Document, Pasadena, CA, 2025.

Kacimi, S., Jaruwatanadilok, S., and Kwok, R.: SWOT Observations Over Sea Ice: A First Look, Geophysical Research Letters, 52, e2025GL116 079, https://doi.org/https://doi.org/10.1029/2025GL116079, e2025GL116079 2025GL116079, 2025.

Kern, M., Cullen, R., Berruti, B., Bouffard, J., Casal, T., Drinkwater, M. R., Gabriele, A., Lecuyot, A., Ludwig, M., Midthassel, R., Navas Traver, I., Parrinello, T., Ressler, G., Andersson, E., Martin-Puig, C., Andersen, O., Bartsch, A., Farrell, S., Fleury, S., Gascoin, S., Guillot, A., Humbert, A., Rinne, E., Shepherd, A., van den Broeke, M. R., and Yackel, J.: The Copernicus Polar Ice and Snow Topography Altimeter (CRISTAL) high-priority candidate mission, The Cryosphere, 14, 2235–2251, https://doi.org/10.5194/tc-14-2235-2020, 2020.

Laloue, A., Schaeffer, P., Pujol, M.-I., Veillard, P., Andersen, O., Sandwell, D., Delepoulle, A., Dibarboure, G., and Faugère, Y.: Merging Recent Mean Sea Surface Into a 2023 Hybrid Model (From Scripps, DTU, CLS, and CNES), Earth and Space Science, 12, e2024EA003 836, https://doi.org/https://doi.org/10.1029/2024EA003836, e2024EA003836 2024EA003836, 2025.

Lin, P., Pickart, R. S., Heorton, H., Tsamados, M., Itoh, M., and Kikuchi, T.: Recent state transition of the Arctic Ocean's Beaufort Gyre, Nature Geoscience, 16, 485–491, https://doi.org/10.1038/s41561-023-01184-5, 2023.

Müller, F. L., Dettmering, D., and Seitz, F.: First arctic-wide assessment of SWOT swath altimetry with ICESat-2 over sea ice, The Cryosphere, 20, 397–409, https://doi.org/10.5194/tc-20-397-2026, 2026.

Peral, E., Esteban-Fernández, D., Rodríguez, E., McWatters, D., De Bleser, J.-W., Ahmed, R., Chen, A. C., Slimko, E., Somawardhana, R., Knarr, K., Johnson, M., Jaruwatanadilok, S., Chan, S., Wu, X., Clark, D., Peters, K., Chen, C. W., Mao, P., Khayatian, B., Chen, J., Hodges, R. E., Boussalis, D., Stiles, B., and Srinivasan, K.: KaRIn, the Ka-Band Radar Interferometer of the SWOT Mission: Design and in-Flight Performance, IEEE Transactions on Geoscience and Remote Sensing, 62, 1–27, https://doi.org/10.1109/TGRS.2024.3405343, 2024.

Tschudi, M., Meier, W., Stewart, J., Fowler, C., and Maslanik, J.: Polar Pathfinder Daily 25 km EASE-Grid Sea Ice Motion Vectors, Version 4, https://doi.org/10.5067/INAWUWO7QH7B, 2019.